

Manuscript Number:

Title: A Cartesian grid embedded boundary method for solving the Poisson and heat equations with discontinuous coefficients in three dimensions

Article Type: Regular Article

Keywords: heat equation; jump conditions; discontinuous coefficient; irregular domain; finite volume methods; multigrid methods

Corresponding Author: Dr. R. K. Crockett,

Corresponding Author's Institution: Lawrence Berkeley National Lab

First Author: R. K. Crockett

Order of Authors: R. K. Crockett; Phillip Colella, Ph.D.; Daniel T Graves, Ph.D.

Abstract: We present a method for solving Poisson and heat equations with discontinuous coefficients in two- and three-dimensions. It uses a Cartesian cut-cell/embedded boundary method to represent the interface between materials, as described in Johansen & Colella (1998). Matching conditions across the interface are enforced using an approximation to fluxes at the boundary. Overall second order accuracy is achieved, as indicated by an array of tests using non-trivial interface geometries. Both the elliptic and heat solvers are shown to remain stable and efficient for material coefficient contrasts up to 10^6 , thanks in part to the use of geometric multigrid. A test of accuracy when adaptive mesh refinement capabilities are utilized is also performed. An example problem relevant to nuclear reactor core simulation is presented, demonstrating the ability of the method to solve problems with realistic physical parameters.

Suggested Reviewers: Randall LeVeque Ph.D.
rjl@amath.washington.edu

Leslie Greengard Ph.D.
greengard@cims.nyu.edu

Donna Calhoun Ph.D.
donna.calhoun@cea.fr

A Cartesian grid embedded boundary method for
solving the Poisson and heat equations with
discontinuous coefficients in three dimensions

R.K. Crockett*, P. Colella, D.T. Graves

*Applied Numerical Algorithms Group, Lawrence Berkeley National Laboratory, MS
50A-1148, 1 Cyclotron Road, Berkeley CA 94720*

Abstract

We present a method for solving Poisson and heat equations with discontinuous coefficients in two- and three-dimensions. It uses a Cartesian cut-cell/embedded boundary method to represent the interface between materials, as described in Johansen & Colella (1998). Matching conditions across the interface are enforced using an approximation to fluxes at the boundary. Overall second order accuracy is achieved, as indicated by an array of tests using non-trivial interface geometries. Both the elliptic and heat solvers are shown to remain stable and efficient for material coefficient contrasts up to 10^6 , thanks in part to the use of geometric multigrid. A test of accuracy when adaptive mesh refinement capabilities are utilized is also performed. An example problem relevant to nuclear reactor core simulation is presented, demonstrating the ability of the method to solve problems with realistic physical parameters.

Key words: heat equation; jump conditions; discontinuous coefficient;

*Corresponding author
Email address: `RKCrockett@lbl.gov` (R.K. Crockett)

1. Introduction

We consider elliptic and parabolic problems in regions with two materials, each of which occupies a bounded subset Ω^p , $p = +, -$, of the overall domain $\Omega = \bigcup_p \Omega^p$. One region usually encloses the other; in that case we refer to the inclusion, or interior region, by Ω^- and the exterior region by Ω^+ . At the boundary $\delta\Omega^\pm$ between materials, jump conditions on the solution φ and flux \mathbf{F}^B are specified

$$\begin{aligned} [\varphi^B] &= \varphi^{B,+} - \varphi^{B,-} = g_D(\mathbf{x}, t) \\ [\mathbf{F}^B \cdot \hat{\mathbf{n}}^B] &= \mathbf{F}^{B,+} \cdot \hat{\mathbf{n}}^B - \mathbf{F}^{B,-} \cdot \hat{\mathbf{n}}^B = g_N(\mathbf{x}, t). \end{aligned} \quad (1)$$

Here $\hat{\mathbf{n}}^B$ is the normal to the boundary, and the functions g_D and g_N describe the magnitude of the jump at each point in time and space. Our method applies to the heat equation in two materials,

$$\partial_t \varphi = \kappa^p \Delta \varphi + f \text{ on } \Omega^p, \quad \varphi(\mathbf{x}, 0) = \varphi_0(\mathbf{x}), \quad (2)$$

subject to the above jump conditions at the interface. In this case, as well as in the elliptic equations to which the method is applied, the flux \mathbf{F}^B is proportional to the material coefficient. While this coefficient is constant within each material, it is discontinuous across the interface.

There are a number of schemes for handling elliptic and parabolic problems of this type extant in the literature. Finite difference schemes for fixed boundaries, of the type pioneered by Shortley & Weller [1], have been greatly improved upon in the intervening years. Most importantly in the context of

1
2
3
4
5
6
7
8
9 this work, they have been extended to handle discontinuous jumps in the
10 form of Equation (10). Immersed boundary methods, modifications of the
11 method first presented by Peskin [2], discretize a delta-function source term
12 on the boundary, retaining the symmetric form of the linear system. Im-
13 mersed interface methods [3] explicitly incorporate the jump condition into
14 the underlying finite difference stencil coefficients. This results in a scheme
15 that more accurately represents the jump conditions, at the expense of con-
16 siderable additional complexity and the loss of symmetry in the underlying
17 linear system. Finally in the context of finite difference schemes, ghost fluid
18 methods [4] use a type of analytic continuation of the solution. A ghost
19 fluid, residing in the regions ostensibly outside the solution domain, is used
20 to explicitly enforce the matching conditions. As originally formulated, the
21 method was first order accurate. It has been extended to second order ac-
22 curacy for boundaries with continuous second derivatives [5]. They have the
23 advantage of retaining a symmetric system, allowing the use of a wider range
24 of fast linear solvers.

25
26
27
28
29
30
31
32
33
34
35
36
37
38
39
40 Outside the realm of finite difference methods, integral methods recast
41 the elliptic PDE via potential theory as integral equations. Fast integral
42 solvers can often be utilized against this class of problem; these generally fall
43 into two categories. One method involves the use of a fast Poisson solver on
44 a simple (e.g. Cartesian) enclosing domain, plus the application of a suitable
45 correction at the boundary [6]. The second combines a fast (e.g. multipole or
46 FFT) method and an iterative solver. In either case, conditioning issues can
47 arise in problems with large discontinuities in the material coefficient [7], ne-
48 cessitating a modification of the underlying integral equation representation.
49
50
51
52
53
54
55
56
57
58
59
60
61
62
63
64
65

1
2
3
4
5
6
7
8
9 Nevertheless, these methods are efficient in a wide variety of problems.

10
11 Our method is based on a finite volume approach to the spatial discretiza-
12 tion of elliptic equations. The method is conservative, a distinct advantage
13 in certain classes of problems. For low-Mach flows with heat transfer, for
14 instance, conservative schemes avoid unphysical results arising in marginally
15 resolved or under-resolved situations [8, 9].

16
17
18
19
20
21 Finite volume methods for interface problems encompass a variety of ap-
22 proaches. In the context of conjugate heat transfer in complex geometries, the
23 overlapping grid method of Henshaw & Chand [10] decomposes the domain
24 into a number of sub-domains. The grid on each sub-domain is boundary
25 fitting, an advantage that comes at the expense of the loss of conservation.
26 Each sub-domain can utilize a solver specific to the physics in it.

27
28
29
30
31
32 Oevermann et al [11, 12] present a finite volume method for variable and
33 discontinuous coefficient elliptic problems in two- and three-dimensions. In 3-
34 D, it relies on tri-linear approximations to the solution within each Cartesian
35 control volume to discretize the integral form of the divergence theorem in
36 a finite element fashion. Small volume cells are handled via an asymptotic
37 approach. The method exhibits local and global second order accuracy on
38 this class of problems.

39
40
41
42
43
44
45 Our work follows in the steps of the work in [13, 14, 15] in using pure
46 finite-volume schemes for elliptic and parabolic equations with embedded
47 boundaries (EB). The first step in using Cartesian EB methods is grid gen-
48 eration, which has been studied extensively using a number of different rep-
49 resentations of the geometry. Surface triangulations [16] are widely used,
50 particularly in engineering contexts involving extremely complex geometries.
51
52
53
54
55
56
57
58
59
60
61
62
63
64
65

1
2
3
4
5
6
7
8
9 Our method uses an implicit function representation [17] that provides dis-
10 cretizations of complex geometries accurate to arbitrary order in a straight-
11 forward manner.
12
13

14
15 The main shortcoming in previous Cartesian EB methods, insofar as their
16 application to multi-material problems, lies in their use of prescribed bound-
17 ary conditions at the EB. A Neumann interface gave boundary fluxes directly,
18 while Dirichlet boundary conditions at the EB necessitated defining a stencil
19 for calculating fluxes at the boundary using data at neighboring cells. In the
20 multi-material context boundary conditions at the interface are not directly
21 prescribed, but instead constrained by matching conditions on the jump in
22 the solution and flux across it. The present work extends the EB methodol-
23 ogy to handle such jump conditions, and thereby solve multi-material Poisson
24 and heat equations with a discontinuity in the material coefficient at the in-
25 terface between the two. Like previous work, it maintains global second order
26 accuracy. By treating special cases related to under-resolved geometries, like
27 the presence of multiple interfaces within a Cartesian control volume, we
28 are able to use geometric multigrid methods for efficient solution of elliptic
29 equations. Moreover, our use of the Chombo software infrastructure provides
30 two important capabilities from a computational efficiency standpoint. The
31 first is adaptive mesh refinement, which is crucial in many problems involv-
32 ing widely separated spatial scales. Second, it provides well tested parallel
33 computing capabilities, which is crucial in approaching real-world problems.
34
35
36
37
38
39
40
41
42
43
44
45
46
47
48
49
50

51 Our time discretization of this equation necessitates solving a set of el-
52 liptic equations during each step forward in time. Specifically, we solve the
53
54
55
56
57
58

Helmholtz equation

$$(\alpha^p + \beta^p \Delta) \varphi = \rho, \quad (3)$$

where α^p and β^p are the material coefficients, subject to jump conditions across the boundary $\delta\Omega^\pm$. We first describe the elliptic algorithm, starting with the spatial discretization in Section 2. This is followed by a treatment of special considerations for the use of geometric multigrid, in Section 3. An outline of the overall algorithm is given in Section 4.

Descriptions of the tests used to validate the method follow the algorithmic sections. These include two and three dimensional solution error tests confirming second order accuracy for the Poisson equation in Section 5.1 and Section 5.3. Tests of the efficiency of the multigrid solver in 2-D and 3-D are described in Section 5.2. The final set of test are of accuracy for the heat equation in 3-D, in Section 5.4. We conclude with results more realistic problem, showing heat conduction in a nuclear reactor fuel assembly, in Section 5.5.

2. Spatial Discretization of the Laplacian

The underlying discretization of space is given by rectangular control volumes on a Cartesian grid: $\Upsilon_{\mathbf{i}} = [(\mathbf{i} - \frac{1}{2}\mathbf{u})h, (\mathbf{i} + \frac{1}{2}\mathbf{u})h]$, $\mathbf{i} \in \mathbb{Z}^d$, where d is the dimensionality of the problem, h is the mesh spacing, and \mathbf{u} is the vector whose entries are all ones. Each material domain Ω^p and material interface $\delta\Omega^{pp'}$ is represented by its intersection with the Cartesian grid. In general, a given Cartesian control volume $\Upsilon_{\mathbf{i}}$ may be intersected by one or more material interfaces. Consequently, there may be multiple p -material control volumes associated with each $\Upsilon_{\mathbf{i}}$; see Figure 1. In the case that

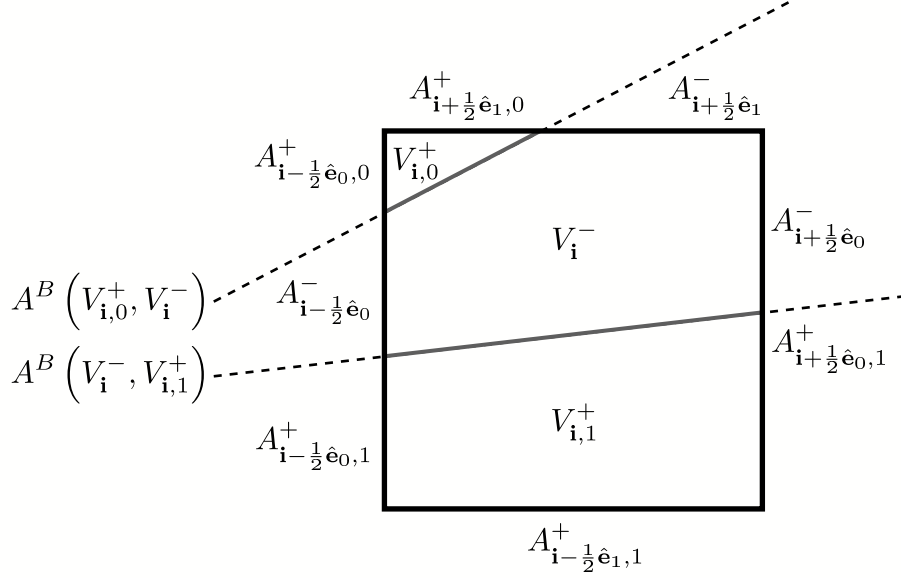


Figure 1: A 2-D Cartesian control volume, and its associated material control volumes. In this case the volume is crossed by two material interfaces. The top region is in the $p = +$ phase, the region below it in phase $p' = -$, and the bottom region in phase $p = +$ again. Each material control volume is labeled by the Cartesian volume containing it, \mathbf{i} , its phase p and, if there are multiple volumes of that phase in the Cartesian volume, the index γ , as $V_{\mathbf{i},\gamma}^p$. Interfaces between material control volumes are shown as solid grey lines, whose areas are labeled A^B . Non-zero faces of the material control volumes, lying on the boundary of the Cartesian control volume, are labeled $A_{\mathbf{i}\pm\frac{1}{2}\hat{\mathbf{e}}_s,\gamma}^p$.

there is more than one p -material control volume in the Cartesian control volume, we index them by $\gamma = 0, 1, \dots$. Each p -material control volume is denoted by $V_{\mathbf{i},\gamma}^p$, and each face by $A_{\mathbf{i} \pm \frac{1}{2}\mathbf{e}_s, \gamma}^p$. The latter is defined as the intersection of Ω^p with $\delta\Upsilon_{\mathbf{i}}$, the boundary of the control volume $\Upsilon_{\mathbf{i}}$ given by the coordinate planes $\{\mathbf{x} : x_s = (i_s \pm \frac{1}{2}\hat{\mathbf{e}}_s)h\}$, where $\hat{\mathbf{e}}_s$ is the unit vector in the s direction. Finally, associated with each Cartesian control volume through which one or more material boundaries passes is a boundary face, or interface, $A_{\mathbf{i}}^{B,p}(V_{\mathbf{i},\gamma}^p, V_{\mathbf{i},\gamma'}^{p'}) = dV_{\mathbf{i},\gamma}^p \cap dV_{\mathbf{i},\gamma'}^{p'} \subset \delta\Omega^{pp'}$ with normal $\hat{\mathbf{n}}_{\mathbf{i},\gamma\gamma'}^{B,p}$ facing out of material p . We assume that each material interface connects a single p -material control volume to a single p' -material control volume. In other words, each p -material interface must be connected in a one-to-one fashion to another face in material $p' \neq p$ having the same spatial location and area fraction, but opposite normal (i.e. $|A_{\mathbf{i}}^{B,p}(V_{\mathbf{i},\gamma}^p, V_{\mathbf{i},\gamma'}^{p'})| = |A_{\mathbf{i}}^{B,p'}(V_{\mathbf{i},\gamma'}^{p'}, V_{\mathbf{i},\gamma}^p)|$ and $\hat{\mathbf{n}}_{\mathbf{i},\gamma\gamma'}^{B,p} = -\hat{\mathbf{n}}_{\mathbf{i},\gamma'\gamma}^{B,p'}$).

The construction of our finite-volume method follows McCorquodale et al [14], with suitable modifications for multi-material equations. Based on the description above, we construct geometric quantities:

- The dimensionless volumes/areas of each p -material control volume/face.
 Volume fractions $\nu_{\mathbf{i},\gamma}^p = |V_{\mathbf{i},\gamma}^p| h^{-d}$, face apertures $\alpha_{\mathbf{i} + \frac{1}{2}\mathbf{e}_s, \gamma}^p = |A_{\mathbf{i} + \frac{1}{2}\mathbf{e}_s, \gamma}^p| h^{-(d-1)}$,
 and boundary apertures $\alpha_{\gamma\gamma'}^{B,p} = |A_{\gamma\gamma'}^{B,p}(V_{\mathbf{i},\gamma}^p, V_{\mathbf{i},\gamma'}^{p'})| h^{-(d-1)}$

- The locations of centroids and average outward normal to the boundary

$$\mathbf{x}_{\mathbf{i},\gamma}^p = \frac{1}{|V_{\mathbf{i},\gamma}^p|} \int_{V_{\mathbf{i},\gamma}^p} \mathbf{x} dV \quad (4)$$

$$\mathbf{x}_{\mathbf{i}+\frac{1}{2}\mathbf{e}_s,\gamma}^p = \frac{1}{|A_{\mathbf{i}+\frac{1}{2}\mathbf{e}_s,\gamma}^p|} \int_{A_{\mathbf{i}+\frac{1}{2}\mathbf{e}_s,\gamma}^p} \mathbf{x} dA \quad (5)$$

$$\mathbf{x}_{\mathbf{i},\gamma\gamma'}^{B,pp'} = \frac{1}{|A^B(V_{\mathbf{i},\gamma}^p, V_{\mathbf{i},\gamma'}^{p'})|} \int_{A^B(V_{\mathbf{i},\gamma}^p, V_{\mathbf{i},\gamma'}^{p'})} \mathbf{x} dA \quad (6)$$

$$\hat{\mathbf{n}}_{\mathbf{i},\gamma\gamma'}^{B,p} = \frac{1}{|A^B(V_{\mathbf{i},\gamma}^p, V_{\mathbf{i},\gamma'}^{p'})|} \int_{A^B(V_{\mathbf{i},\gamma}^p, V_{\mathbf{i},\gamma'}^{p'})} \hat{\mathbf{n}}^{B,p} dA, \quad (7)$$

where $\hat{\mathbf{n}}^{B,p}$ is the normal, facing outward from phase p , to $\delta\Omega^{pp'}$, defined at each point on $\delta\Omega^{pp'}$.

Finite volume methods are based on the divergence form of the underlying equation, which we now recast in terms of the above defined geometric quantities. For the Poisson (heat) equation, the divergence form is $\nabla \cdot \mathbf{F} = \rho$ ($\nabla \cdot \mathbf{F} = \partial_t \varphi - f$), with $\mathbf{F} = \beta \nabla \varphi$ ($\mathbf{F} = k \nabla \varphi$). Our conservative discretization for the divergence operator in each material control volume $V_{\mathbf{i},\gamma}^p$ is

$$\begin{aligned} (\nabla \cdot \mathbf{F})_{\mathbf{i},\gamma}^p &\approx \frac{1}{V_{\mathbf{i},\gamma}^p} \int_{V_{\mathbf{i},\gamma}^p} \nabla \cdot \mathbf{F} dV = \frac{1}{V_{\mathbf{i},\gamma}^p} \int_{\delta V_{\mathbf{i},\gamma}^p} \mathbf{F} \cdot \hat{\mathbf{n}} dA \\ &\simeq \frac{1}{\nu_{\mathbf{i},\gamma}^p h} \left[\sum_{\pm=+,-} \sum_{s=1}^d \pm \alpha_{\mathbf{i}+\frac{1}{2}\mathbf{e}_s,\gamma}^p F^{s,p}(\mathbf{x}_{\mathbf{i}+\frac{1}{2}\mathbf{e}_s,\gamma}) + \sum_{\substack{p' \neq p \\ \gamma'}} \alpha_{\mathbf{i},\gamma\gamma'}^{B,pp'} F^{B,p}(\mathbf{x}_{\mathbf{i},\gamma\gamma'}^{B,pp'}) \right]. \end{aligned} \quad (8)$$

Here $F^{s,p}(\mathbf{x})$ is the flux from the p -material through the face with normal \mathbf{e}_s at position \mathbf{x} , and $F^{B,p}$ is the corresponding flux through the material boundary. So, for example, in the material control volume at upper-right in

Figure 1, the divergence is

$$(\nabla \cdot \mathbf{F})_{i,0}^+ = \frac{1}{\nu_{i,0}^+ h} \left[\alpha_{i-\frac{1}{2}\mathbf{e}_0,0}^+ F^{0,+}(\mathbf{x}_{i-\frac{1}{2}\mathbf{e}_0,0}) - \alpha_{i+\frac{1}{2}\mathbf{e}_1,0}^+ F^{1,+}(\mathbf{x}_{i+\frac{1}{2}\mathbf{e}_1,0}) \right. \\ \left. + \alpha_{i,00}^{B,+} F^{B,+}(\mathbf{x}_{i,00}^{B,+}) \right] \quad (9)$$

Thus, with the discretization in place, we need to calculate fluxes at all faces and boundaries in order to update the governing equation.

2.1. Flux calculation and enforcing multi-material matching conditions

The Laplacian operator in the Poisson (heat) equation implies a flux $\mathbf{F}^p = \beta^p \nabla \varphi$ ($\mathbf{F}^p = \kappa^p \nabla \varphi$). Calculation of fluxes at faces $A_{i+\frac{1}{2}\mathbf{e}_s,\gamma}^p$ is a relatively straightforward matter of linearly interpolating fluxes at face centers to the face centroids $\mathbf{x}_{i+\frac{1}{2}\mathbf{e}_s,\gamma}^p$; an example is given in [14], Equations (6) and (7). For interfaces A^B , the process is more involved. First let us introduce simplified notation,

$$\hat{\mathbf{n}}^{B,p} \cdot \mathbf{F} = \hat{\mathbf{n}}^{B,p} \cdot (\beta \nabla \varphi)^{B,p} \equiv \beta^p \frac{\partial \varphi^{B,p}}{\partial n}. \quad (10)$$

In the single-material case [14, 15], Neumann or Dirichlet boundary conditions are prescribed at the interface. In the former case, the required interface flux \mathbf{F}^B can be calculated directly. In the Dirichlet case, the state at the interface, φ^B , and at neighboring cells is used to approximate the normal derivative at the interface $\frac{\partial \varphi}{\partial n}$. In the multi-material case, neither Dirichlet nor Neumann boundary conditions at the interface are known a priori. Instead, we use the matching conditions, Equation (10), along with equations approximating the normal derivative in each material, in order to calculate the boundary flux in Equation (8).

We illustrate the flux determination for the case of the Poisson equation in two materials. (The same procedure applies to the Helmholtz equation

solves done in the heat equation update.) First, we rewrite the second (flux) jump condition of Equation (10) as

$$\beta^+ \frac{\partial \varphi^{B,+}}{\partial n} - \beta^- \frac{\partial \varphi^{B,-}}{\partial n} = g_N. \quad (11)$$

The states in either material at the interface, φ^B , and normal derivatives, $\frac{\partial \varphi^B}{\partial n}$, are not known. Our method for closing this set of equations is to use an approximation to the normal derivative of the form

$$\frac{\partial \varphi^{B,p}}{\partial n} = w^{B,p} \varphi^{B,p} + \sum_{\mathbf{i} \in \Omega^p} w_{\mathbf{i}} \varphi_{\mathbf{i}} + \mathbf{O}(h^q), \quad (12)$$

where q is the order of approximation. The weight w^B associated with the unknown boundary state, and $w_{\mathbf{i}}$ associated with the known states in neighboring cells depend on the geometric quantities defined in Equations (4-7). In general, a second order approximation [13] to the normal derivative is used. In cases where there are insufficient neighboring cells $\varphi_{\mathbf{i}}$ for a second order approximation (e.g. due to an under-resolved geometry, or proximity to the domain boundary), a first order approximation [15] is used.

Since we are using two different approximation schemes it remains to show here that, independent of which combination of approximation schemes is used on either side of the interface, the matching conditions can still be enforced. We do so by showing that both can be recast in the form Equation (12) given above. Clearly, given its linear dependence on φ^B , this allows a simple direct solution of the four-by-four system for φ^B and $\frac{\partial \varphi^B}{\partial n}$ on both sides of the material boundary.

First, consider the second-order stencil based on the quadratic interpolation of two values, φ_1 and φ_2 , at distances d_1 and d_2 along the normal to the

interface,

$$\frac{\partial \varphi^B}{\partial n} = \frac{1}{d_2 - d_1} \left(\frac{d_2}{d_1} (\varphi^B - \varphi_1) - \frac{d_1}{d_2} (\varphi^B - \varphi_2) \right). \quad (13)$$

The two state values φ_1 and φ_2 depend on geometric quantities and the states in neighboring cells, but not φ^B . Therefore, it is a simple matter to rewrite this equation in the form above

$$\frac{\partial \varphi^B}{\partial n} = \frac{1}{d_2 - d_1} \left(\frac{d_2}{d_1} - \frac{d_1}{d_2} \right) \varphi^B + \frac{1}{d_2 - d_1} \left(\frac{d_1}{d_2} \varphi_2 - \frac{d_2}{d_1} \varphi_1 \right) \quad (14)$$

$$= w^B \varphi^B + \sum_{\mathbf{i} \in \Omega_1} w_{\mathbf{i}} \varphi_{\mathbf{i}} + \sum_{\mathbf{i} \in \Omega_2} w_{\mathbf{i}} \varphi_{\mathbf{i}}, \quad (15)$$

where Ω_1 and Ω_2 correspond to the domain of dependence used in calculating φ_1 and φ_2 . This is clearly in the form of Equation (12).

In the alternative case, when a suitable second order approximation is not available, we use the Schwartz et al prescription for calculating the normal derivative, based on least squares estimation. This method involves choosing a suitable set of neighboring points - three in the case of 2-D, and seven in 3-D - for performing least squares estimation. A matrix of displacements of these points from the material interface is defined, $(\mathbb{A})_{s\mu} = \delta x_s^\mu$, where μ indexes the points and s indexes direction. Next define a vector of differences between the state at each point, φ^μ , and the state at the boundary, φ^B : $(\delta\varphi)^\mu = (\varphi)^\mu - \varphi^B$. We wish to solve $\mathbb{A} \nabla \varphi = \delta\varphi$ in order to obtain an estimate for $\frac{\partial \varphi}{\partial n} = \hat{\mathbf{n}} \cdot \nabla \varphi$. We compute the least squares estimate

$$\begin{aligned} \nabla \varphi &\approx (\mathbb{A}^T \mathbb{A})^{-1} \mathbb{A}^T \delta\varphi = (\mathbb{A}^T \mathbb{A})^{-1} \mathbb{A}^T (\varphi - \varphi^B \mathbf{u}) \\ &= \left((\mathbb{A}^T \mathbb{A})^{-1} \mathbb{A}^T \mathbf{u} \right) \varphi^B + (\mathbb{A}^T \mathbb{A})^{-1} \mathbb{A}^T \varphi. \end{aligned} \quad (16)$$

An expression for the normal derivative can then be constructed

$$\begin{aligned}\frac{\partial \varphi}{\partial n} &= \hat{\mathbf{n}} \cdot \nabla \varphi = - \left(\hat{\mathbf{n}}^T (\mathbb{A}^T \mathbb{A})^{-1} \mathbb{A}^T \mathbf{u} \right) \varphi^B + \hat{\mathbf{n}}^T (\mathbb{A}^T \mathbb{A})^{-1} \mathbb{A}^T \varphi \\ &= w^B \varphi^B + \sum_{\mathbf{i}} w_{\mathbf{i}} \varphi_{\mathbf{i}}.\end{aligned}\tag{17}$$

The last step follows from the association of the components of the vector φ with the neighboring state values, $\varphi_{\mathbf{i}}$, and the matrix product $\hat{\mathbf{n}}^T (\mathbb{A}^T \mathbb{A})^{-1} \mathbb{A}^T \mathbf{u}$ with the scalar w^B .

We therefore have two formulae for approximating the normal derivative, both of which are linear in φ^B . Consequently, we are able to solve the jump conditions for $\frac{\partial \varphi}{\partial n}$ by solving a two-by-two system directly. From these we calculate boundary fluxes \mathbf{F}^B , which are used in performing Gauss-Seidel relaxation in each phase. In order that the matching conditions are always satisfied, boundary fluxes are recalculated after every step in relaxing towards the solution of our elliptic equation.

3. Multigrid solver considerations

In order to speed the elliptic equation solver, the relaxation step is embedded in a multigrid solver. This also has the advantage of being highly compatible with adaptive mesh refinement. Use of a multigrid solver involves progressive coarsening of the problem domain, and the geometry along with it. Generally, the further one coarsens in multigrid, the larger the benefit in terms of solver efficiency. The extent to which one can coarsen is limited, however, by the need for an adequate number of cells with which to create a stencil for estimating the flux. This domain coarsening can lead to pathological cases, which we describe and outline our approach to below.

1. Failure of the least squares stencil

In this case, we use least squares, but instead of including only those nearest neighbors within the same quadrant (octant in 3D) as the normal vector, we include all nearest neighbors to which there exists a monotone path from the VoF in question.

We find that this method allows coarsening to levels not possible using the least squares stencil as described above. Moreover, it is useful in preserving symmetry in cases where the boundary normal is along a cardinal direction. It has little effect on the overall accuracy of the scheme, which remains second order in our tests.

2. VoFs missing one or more stencils

Occasionally, at some level in the coarsening, no stencil is available on one or both sides of the interface, and we are left with a choice. One option is to stop coarsening and back up to a finer level at which stencils are available. Another is to fashion a suitable approximation for these under-resolved cases.

In the case that one side of an interface is without a stencil, we are unable to solve the matching conditions in the manner outlined in Section 2.1. Therefore, we approximate the gradient on the side with the stencil directly, taking a simple finite difference using the available cells in that material,

$$(\nabla\varphi)_s = \pm \frac{\varphi_{\mathbf{i} \pm \hat{\mathbf{e}}_s} - \varphi_{\mathbf{i}}}{h}, \quad (18)$$

where $\hat{\mathbf{e}}_s$ is the unit vector in the s direction, and either the backward- or forward-difference is used based on the availability of data φ . We arrive at an estimate of the flux in material p by using the normal to

the interface, $\frac{\partial \varphi^{B,p}}{\partial n} = \hat{\mathbf{n}}^{B,p} \cdot \nabla \varphi$. Using this estimate of the flux in phase p , we then calculate the jump in phase p' :

$$\frac{\partial \varphi^{B,p'}}{\partial n} = \frac{1}{\beta^{p'}} \left(\beta^p \frac{\partial \varphi^{B,p}}{\partial n} + g_N \right). \quad (19)$$

Cases where there is no available stencil on either side of a material interface are rare, even when the geometry is quite under-resolved. In practice, we avoid them by limiting the degree of coarsening the multigrid solver performs, which in turn limits the extent of under-resolution of the geometry. This has the potential to make multigrid less efficient. However, we show in Section 5.2 that it remains efficient across a range of resolutions, even for quite complex geometries.

3. Cells with multiple VoFs

Coarsening of the domain for multigrid can also produce cells with more than one volume of fluid (VoF) of a given phase. One very simple example is an inclined ellipsoid with a large axis ratio. With enough coarsening, the minor axis of the ellipsoid becomes smaller than the grid spacing, leading to a situation like that pictured in Figure 2. In the figure on the right, the VoF in the interior has two irregular faces. Fluxes, and therefore normal derivatives, must be calculated for each separately. These are used to calculate an irregular flux for the VoF, which we label with cell index \mathbf{i} and VoF index γ . For the sake of efficiency and simplicity, however, we do not store all values of the flux F^B and material aperture α^B for a given VoF. Instead we store a single flux and a single aperture from which the update can be calculated.

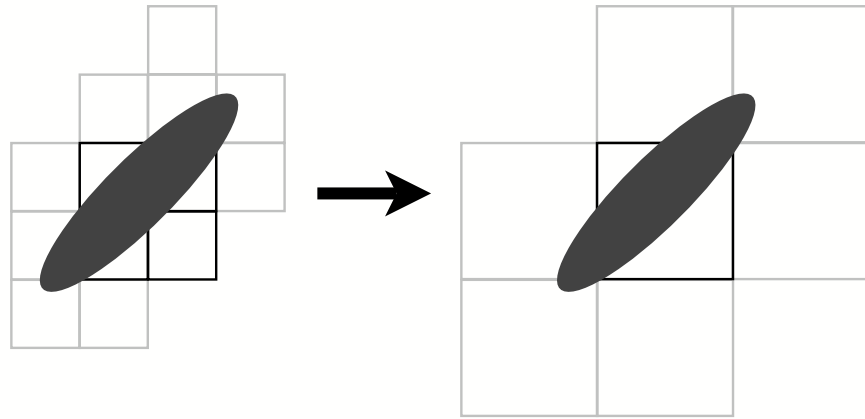


Figure 2: Example of a coarsening resulting in multiple VoFs in a single rectangular control volume. On the left, the cells in black contain a single VoF of each material. After coarsening, the grid is as on the right, with the cell outlined in black having two VoFs of one material, and a single VoF of the other material.

Following Equation (8), we can calculate this single flux as

$$\frac{\partial \varphi^{B,p}}{\partial n_{\mathbf{i},\gamma}} = \frac{\sum_{\gamma'} \alpha_{\mathbf{i},\gamma\gamma'}^{B,pp'} \hat{\mathbf{n}}_{\mathbf{i},\gamma\gamma'} \cdot \mathbf{F}_{\gamma}^{B,p}(\mathbf{x}_{\gamma\gamma'}^{B,pp'})}{\bar{\alpha}_{\mathbf{i},\gamma}^B}. \quad (20)$$

Here the denominator $\bar{\alpha}_{\mathbf{i},\gamma}^B$ is an average material face aperture. The total flux into the VoF is calculated using this single value

$$F_{\mathbf{i},\gamma}^{B,p} = \bar{\alpha}_{\mathbf{i},\gamma}^B \frac{\partial \varphi^B}{\partial n_{\mathbf{i},\gamma}} \quad (21)$$

recovering the correct flux through all irregular faces.

4. Time discretization and algorithm outline

We follow [14] in using a second order in time Runge-Kutta solver [18] in solving the heat equation. The time discretization is

$$T^{n+1} = (\mathbb{I} - \mu_1 \mathbb{L})^{-1} (\mathbb{I} - \mu_2 \mathbb{L})^{-1} \left[(\mathbb{I} + \mu_3 \mathbb{L}) T^n + (\mathbb{I} + \mu_4 \mathbb{L}) f^{n+\frac{1}{2}} \right], \quad (22)$$

with the μ parameters chosen so as to simultaneously achieve second order accuracy and L_0 stability.

The heat equation algorithm proceeds as follows, omitting details of the multigrid operations:

1. Grid generation
 - (a) Calculation of geometric quantities
 - (b) Calculation of stencil weights
2. Heat equation update step solve
 - (a) Calculate source term at half-timestep, $f^{n+\frac{1}{2}}$
 - (b) Apply μ_4 operator

- (c) Apply μ_3 operator
- (d) Solve elliptic problem for μ_2 operator
 - i. Calculate boundary fluxes
 - ii. Single relaxation step in each material
 - iii. Repeat (i) and (ii) to convergence
- (e) Solve elliptic problem for μ_1 operator

Elliptic solver operations form the bulk of the computational work. In order to speed convergence, we plan to investigate the need for performing step (i) before every relaxation step. We leave this investigation for future work, however.

5. Numerical results

5.1. 2-D tests of solution error for Poisson's equation on fixed and adaptive meshes

As a 2-D test of the elliptic solver with a non-trivial geometry, we solve the Poisson equation $\beta\Delta\varphi = \rho$ on a single grid, with two materials whose boundary is a rhodonea curve, originally due to Li [19]. The equation for this curve in polar coordinates is

$$r = r_0 + r_1 \sin(\omega\theta), \quad (23)$$

where r_0 and r_1 are the inner- and outer-radii respectively, and ω the number of lobes of the rhodonea (See Figure 3). Our tests use $r_0 = 0.5$, $r_1 = 0.1$, and $\omega = 5$, as in previous work. Note that the rhodonea is slightly offset from the origin of the domain, being centered at $x = y = 0.2/\sqrt{20}$. We label

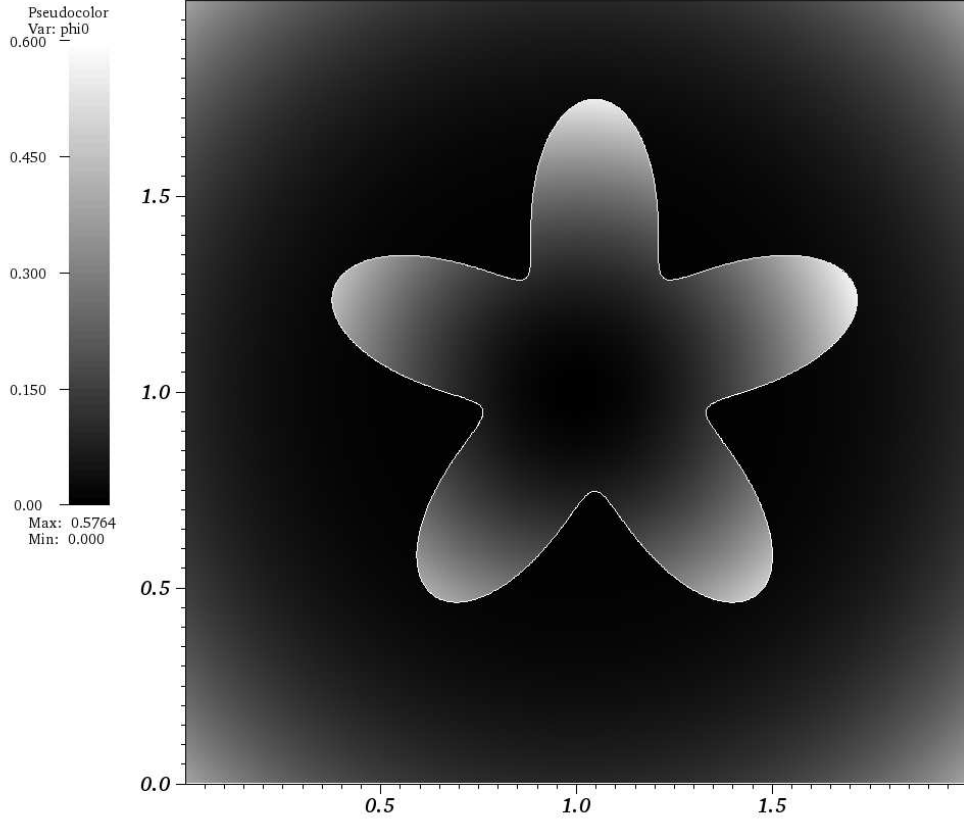


Figure 3: Rhodonea geometry, outlined in white, showing the solution to Poisson's equation inside and outside, with $\beta^- = 10^0$ and $\beta^+ = 10^1$.

quantities on the interior of the rhodonea, the inclusion region, with a minus, such as β^- . Similarly for the exterior, using β^+ .

This example is a good test of the EB methodology due to the high curvature near the inner radius. For the purpose of comparison, we use reproduce Example 2 of [11]. Here, as there, a range of coefficient ratios, $\beta^-/\beta^+ = 10^{-3}$, 10^{-1} , and 10^3 was run. The exact solution is given by

$$\varphi^{ex,+} = \frac{r^4 + c_0 \log(2r)}{\beta^+} \quad (24)$$

$$\varphi^{ex,-} = \frac{r^2}{\beta^-}, \quad (25)$$

from which we calculate the solution error $e_i = \kappa_i(\varphi_i - \varphi_i^{ex})$. Plots of the norm of the solution error and the error in the magnitude of the gradient of the solution (again weighted by volume fraction) are shown in Figure 4. Both are second order accurate in 1-, 2-, and max-norm. Especially noteworthy is the second order convergence of the gradient error, which compares favorably with [11].

The second test uses the same rhodonea geometry, and targets the adaptive mesh refinement (AMR) capabilities of Chombo in the multi-material context. It involves a quadratic source in the center of the rhodonea

$$\rho = \beta^p (a - a^2)^4 \quad (26)$$

$$\varphi^{ex} = \begin{cases} r_0^2 [a^6 (c_4 a^4 + c_3 a^3 + c_2 a^2 + c_1 a + c_0) \\ \quad - (c_4 + c_3 + c_2 + c_1 + c_0) \\ \quad + c \log(r_0)] & \text{if } a < 1 \\ r_0^2 (c \log(r)) & \text{otherwise} \end{cases}, \quad (27)$$

a problem adapted from [14]. Here $a = r/r_0$ and we use a value of $r_0 = 0.2$. The constants are $c = \frac{1}{10} - \frac{4}{9} + \frac{6}{8} - \frac{4}{7} + \frac{1}{6}$, $c_0 = \frac{1}{36}$, $c_1 = -\frac{4}{49}$, $c_2 = \frac{6}{64}$,

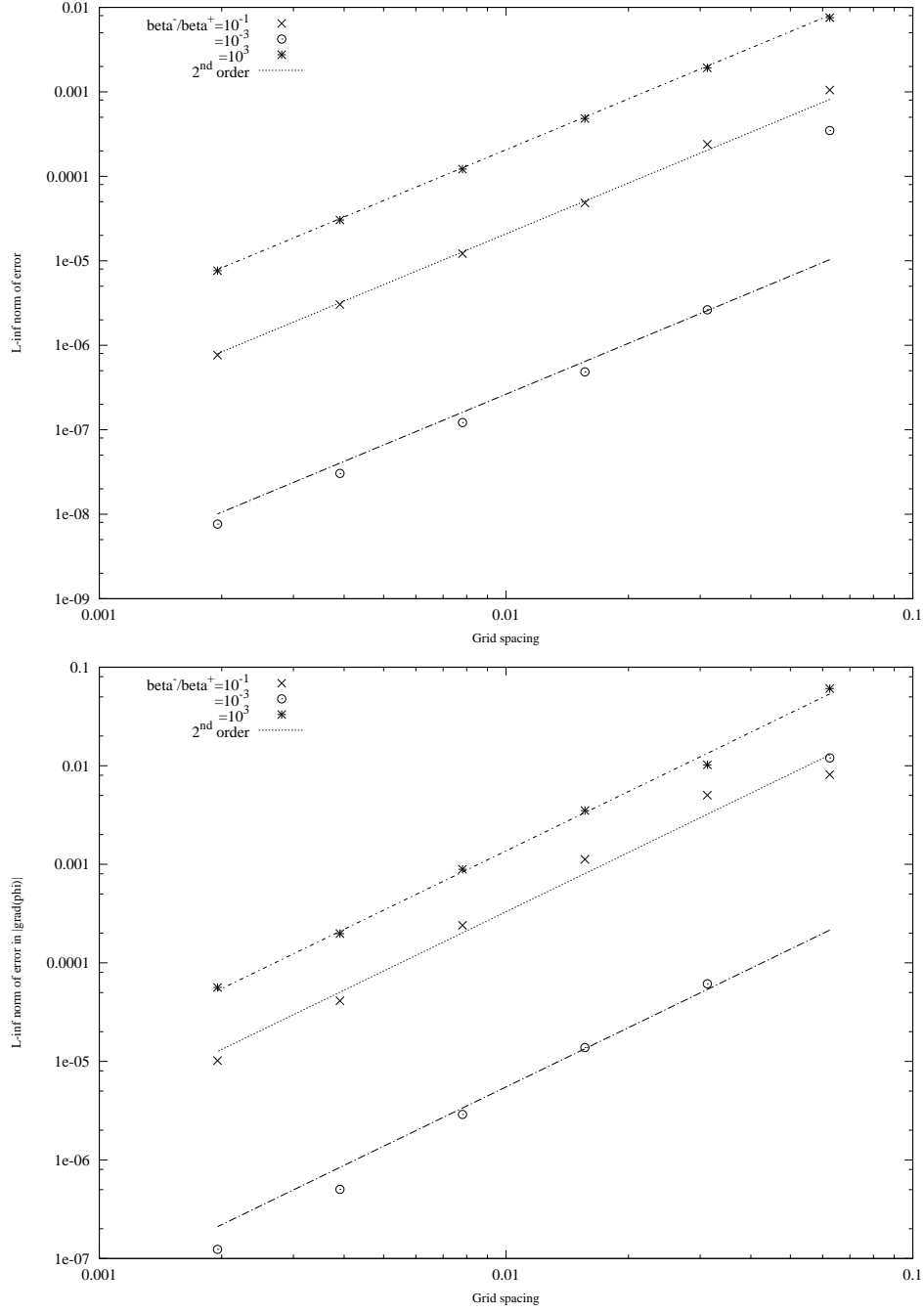


Figure 4: Solution error convergence for the rhodonea example, following Oevermann et al. Top: L_∞ norm of the error in the solution. Note that L_1 and L_2 norms also converge at second order. Bottom: L_∞ norm of the error in the magnitude of the gradient of the solution. Here again, the L_1 and L_2 norms also converges at second order.

$c_3 = -\frac{4}{81}$, and $c_4 = \frac{1}{100}$. We use a modest ratio of $\beta^-/\beta^+ = 1/10$. The matching conditions at the boundary are homogeneous.

Our strategy is to use a single level run to verify the results from an AMR run, in this case with two levels of refinement. With effective gridding, normed errors in the AMR case should be very similar to those of the single grid case with equivalent resolution. We found it simplest to cover the inner ($r < r_0$) region of the rhodonea entirely with the level two and three grids in order to ensure that the region with the largest solution gradient is at the highest resolution. Level two and level three grids also cover the boundary, which is the other large error region. (An alternate strategy for controlling grid placement, Richardson error extrapolation, is more algorithmically complex, and is left for future work.)

Successive AMR runs increase the base level resolution while keeping the number of levels fixed. By comparing the error from these runs with that of single grid runs with equivalent effective resolution, we are able to verify that AMR is not introducing spurious errors. A plot of the error for a R_{128} base grid (effective resolution R_{512}) is shown in Figure 5, top. As shown in the bottom plot, the AMR results are second order. Just as importantly, the magnitude of the normed errors are only marginally higher than those of the single grid calculations.

5.2. 2-D and 3-D tests of multigrid solver efficiency

Here we test the performance of the multigrid solver for a range of grid sizes and beta ratios. In this case an ellipsoid geometry that is easily generalized to three dimensions, as opposed to a 2-D rhodonea geometry, is used. There is no refinement of the domain using AMR. We measure the number

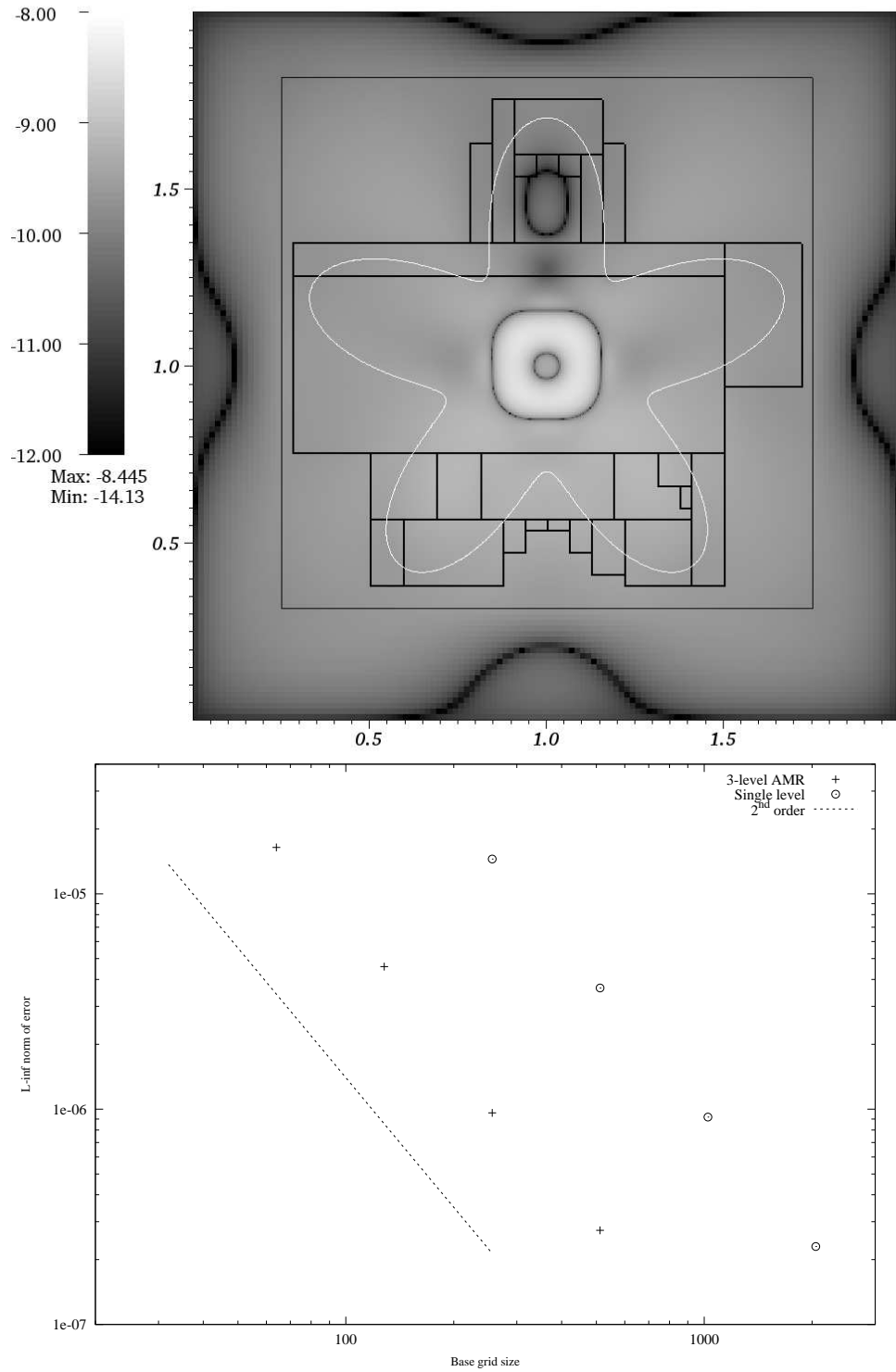


Figure 5: Top: Plot of the log of the magnitude of the error for the AMR test with rhodonea geometry. The rectangle with a thin bounding line shows the extent of the single level two grid. The rectangles with thick bounding lines show the extent of the level three grids. Bottom: L_∞ norm of the error for three level AMR (pluses), and single level (open circles) calculations versus base grid size. The line is a reference showing second order convergence.

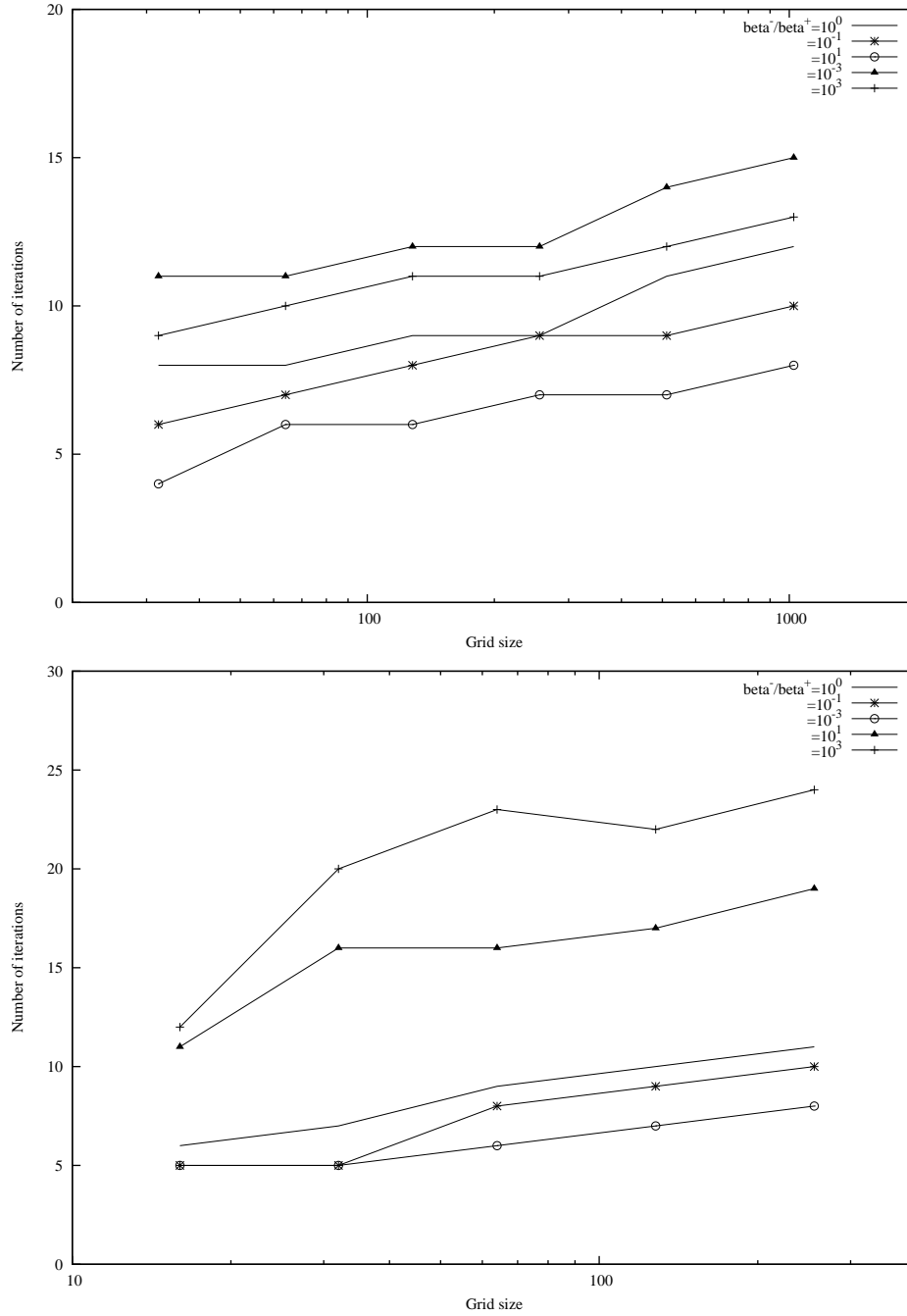


Figure 6: Number of iterations required for convergence versus grid size for an ellipsoid geometry. Beta ratios in the range 10^{-3} to 10^3 are plotted. Top is the 2-D result, and the bottom 3-D. In general, efficiency shows a weak dependence on grid size. At higher beta ratios, however, the dependence is stronger.

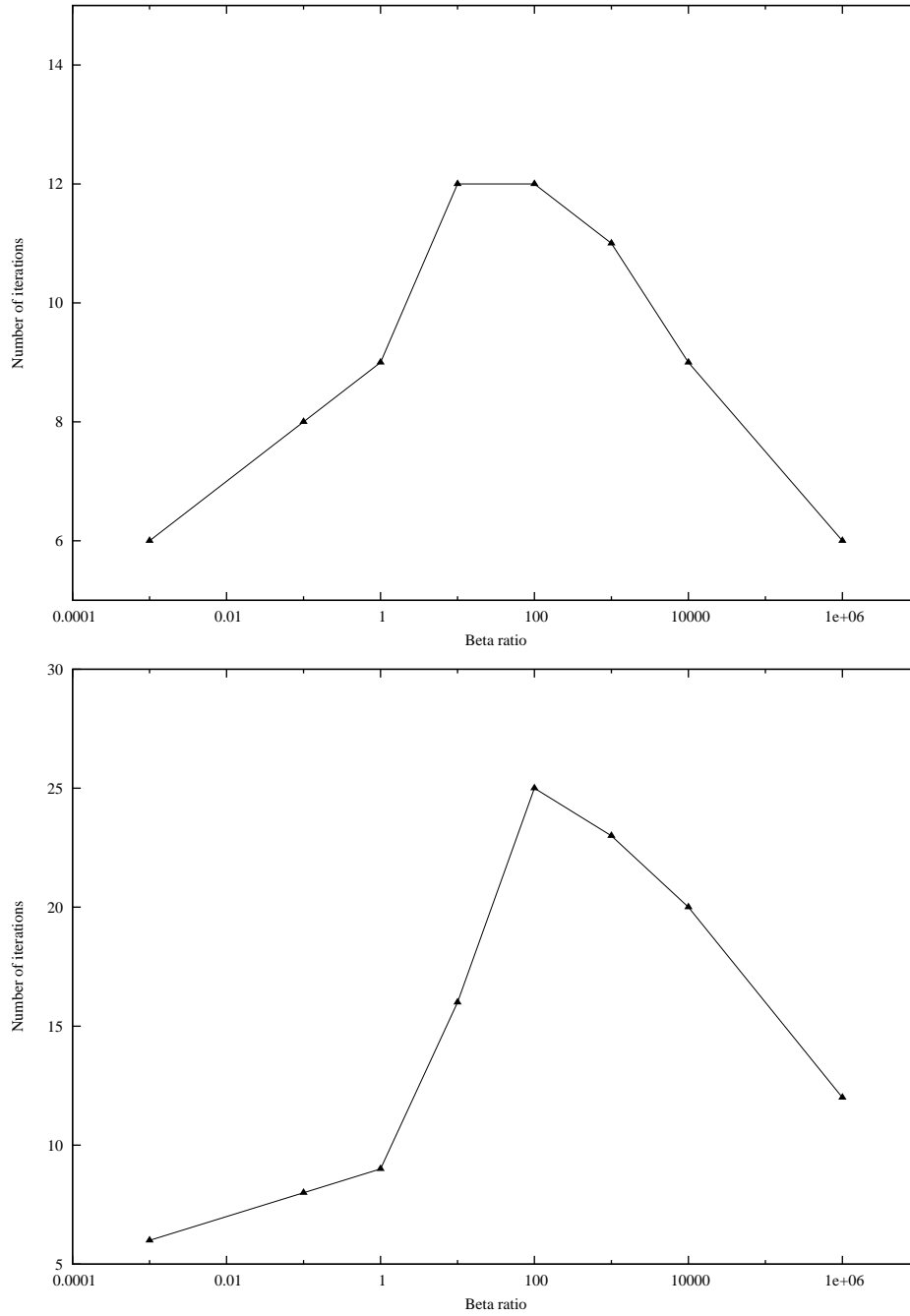


Figure 7: Number of iterations required for convergence versus beta ratio for an ellipsoid geometry. A higher ratio corresponds to a more nearly homogeneous Neumann boundary condition on the interior of the interface. Top is the 2-D result, using a grid size of 128; Bottom is the 3-D results, with a grid size of 64. While convergence initially slows as the beta ratio increases above unity, the effect reverses at ratios above 10^2 .

of multigrid iterations required to reduce the L_2 norm of the error by ten orders of magnitude. Optimally, the iteration count is independent of the grid size. In Figure 6 we plot the iteration count versus grid size for resolutions in the range R_{32} to R_{1024} in the 2-D case, and R_{16} to R_{256} in the 3-D case. The figure shows results for beta ratios from $\beta^-/\beta^+ = 10^{-3}$ to 10^3 . Though the iteration count increases somewhat with increasing grid size, there is a stronger dependence on beta ratio, particularly when the latter is greater than one. The difficulty of solving problems with large beta inclusions is well documented in the literature; see [11, 7]. We have explored this issue further by running over a larger range in beta ratios for a single resolution – R_{128} in 2-D and R_{64} in 3-D. As we show in Figure 7, the iteration count reaches a maximum at a ratio around 10^2 , and decreases thereafter. The multigrid solver performs better than might naively be expected as the beta ratio increases, being well suited for problems with high beta inclusions of 10^6 , and likely even higher.

5.3. 3-D test of solution error for Poisson's equation

Our test of solution error convergence in three dimensions uses a sphere of radius $R = 0.392$, and a source and exact solution proportional to an eigenfunction of the Laplacian in spherical coordinates:

$$\rho(r) = -k^2 \frac{\sin(kr)}{r} \quad (28)$$

$$\varphi^{ex,p}(r) = \frac{1}{\beta^p} \frac{\sin(kr)}{r} + c^p \quad (29)$$

The constant c^p is chosen such that $[\varphi^{ex}] = 0$, giving homogeneous matching conditions at the material boundary. Results for solution error are shown

in Figure 8 and Figure 9. Convergence is second order, independent of the norm and beta ratio chosen.

5.4. 3-D tests of solution error for the heat equation

In order to test the accuracy of our multi-material method for the heat equation, we once again use the method of manufactured solutions. For the desired exact solution φ^{ex} of Equation (2) in material p we again choose for the spatial component the trigonometric eigenfunction of the spherical Laplacian from Section 5.3. Time dependence is added via an exponential decay term. The source term f^p is chosen such the heat equation is satisfied. The exact solution and source are of the form

$$\varphi^{ex,p} = c_0^p \frac{\sin(kr)}{r} e^{-\gamma t} + c_1^p \quad (30)$$

$$f^p = c_0^p (\kappa^p k^2 - \gamma) \frac{\sin(kr)}{r} e^{-\gamma t}. \quad (31)$$

In all cases we choose $k = 2\pi$. The interface between materials is also a sphere of radius $R = 0.392$.

Due to the difficulty of choosing solutions such that the matching conditions Equation (10) are simultaneously zero, we test each in turn. In other words, we perform one test with a homogeneous Dirichlet boundary, where the solution in each phase is the same while the jump in the flux varies in both time and space. The other test uses a homogeneous Neumann boundary, where $\kappa^+ \varphi^+ = \kappa^- \varphi^-$ so that the flux is continuous across the boundary.

For the homogeneous Dirichlet case we use $c_0^- = c_0^+ = 10$, $c_1^- = c_1^+ = 100$, and $\gamma = \max(\kappa^+, \kappa^-)$. All simulations were run for the same number of timesteps, to a final time such that $\gamma t_{final} = 0.2$. For the homogeneous Neumann case we use $c_0^\pm = 10/\kappa^\pm$, with all other parameters the same as in

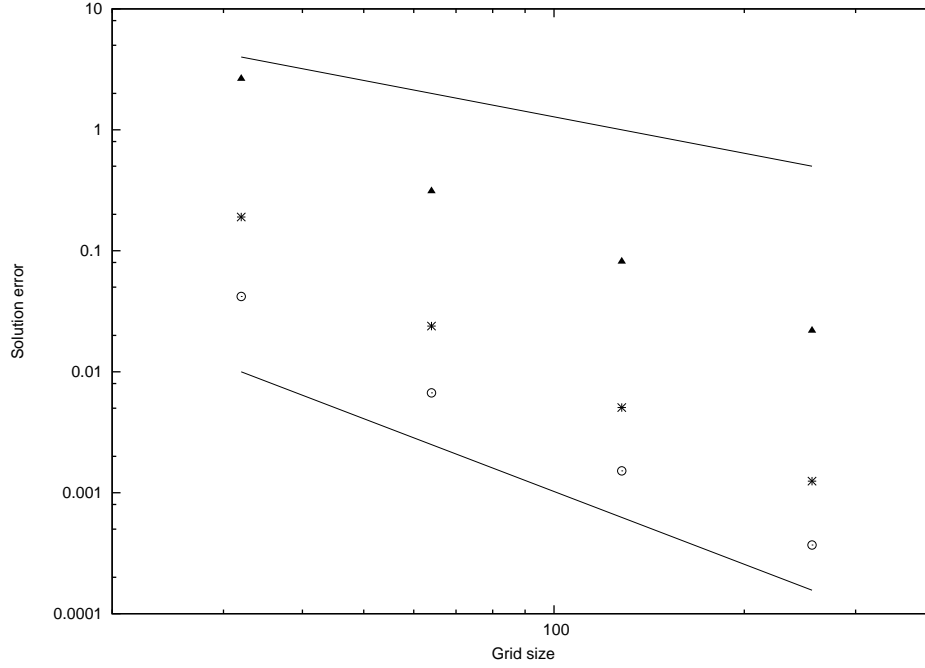


Figure 8: Convergence of the solution error for the Poisson equation in three dimensions with a spherical boundary between materials. The coefficient in the inclusion is $\beta^- = 1$, and on the exterior it is $\beta^+ = 10$. The source and domain boundary conditions are chosen such that the jump conditions are homogeneous. Norms of the solution error are plotted, with triangles denoting the L_∞ norm, stars L_1 , and circles L_2 norm. The top line is a reference showing first-order convergence, and the bottom line showing second-order convergence.

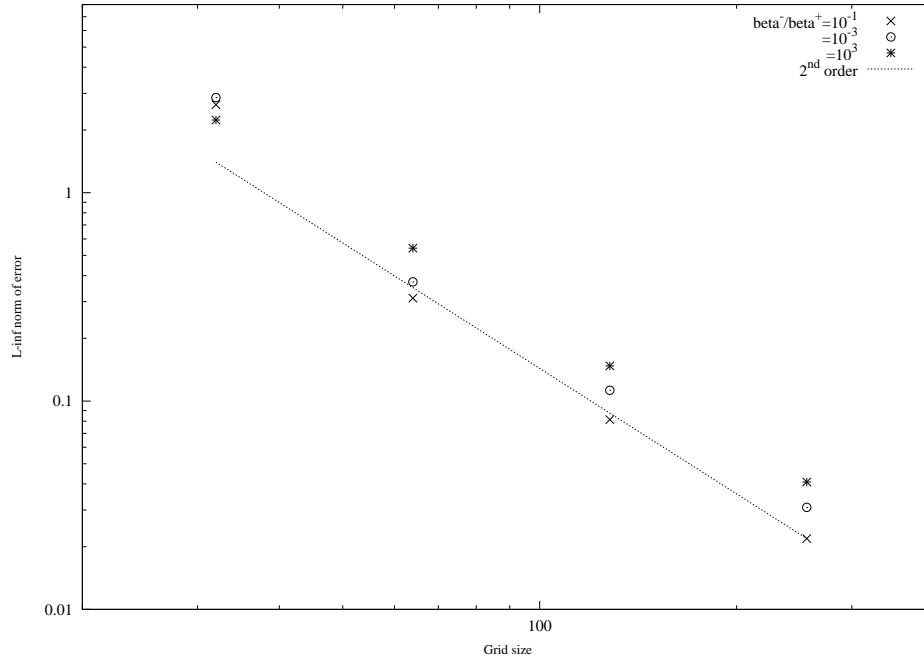


Figure 9: Convergence of the L_∞ norm of the solution error for the Poisson equation in three dimensions, across a range in coefficient ratios. Pluses show a ratio β^-/β^+ of one. Open circles show the case with high beta on the outside, while filled circles show high beta on the inside. The line is a reference showing second-order convergence.

the homogeneous Dirichlet case. Results for solution error convergence are shown in Figure 10, and confirm second order accuracy for both cases.

5.5. Conjugate heat transfer in a nuclear reactor fuel bundle

Finally, we test the multi-material method on a more realistic example, inspired by nuclear reactor core simulation. The geometry consists of a set of nineteen coaxial reactor fuel pins. Each pin is wrapped in a helical wire. Outside of the fuel pin is a moderator, in this case a stationary material with thermal properties equivalent to liquid sodium. The geometric parameters used closely follow [20], and are listed in Table 1.¹ All parameters are in CGS units. The source was a Gaussian that falls off with distance from the pin axis,

$$\tilde{f} = \frac{f}{\rho c_P} = \tilde{F} \exp(-r_{pin}^2/s^2). \quad (32)$$

The source strength $\tilde{F} = 2.5 \times 10^3$, and the width parameter $s = 1/4$. This choice provides a steady-state power density of approximately 10^2 W/m². Initially, the temperature is uniform at 600 K. The top and bottom domain boundaries were adiabatic ($\frac{\partial T}{\partial z} = 0$), while the others were kept constant at 600 K. The simulation was run using timesteps of $dt = 0.1$ to a final time of $t = 51.0$, at which point the heat flux through the boundary had reached a steady state. Figure 11 shows the temperature distribution at this final time.

¹The value of the thermal diffusivity in the pins was inferred. Specifically, the sodium (moderator) thermal conductivity listed in [21] was multiplied by the ratio of pin to moderator conductivities used in [10].

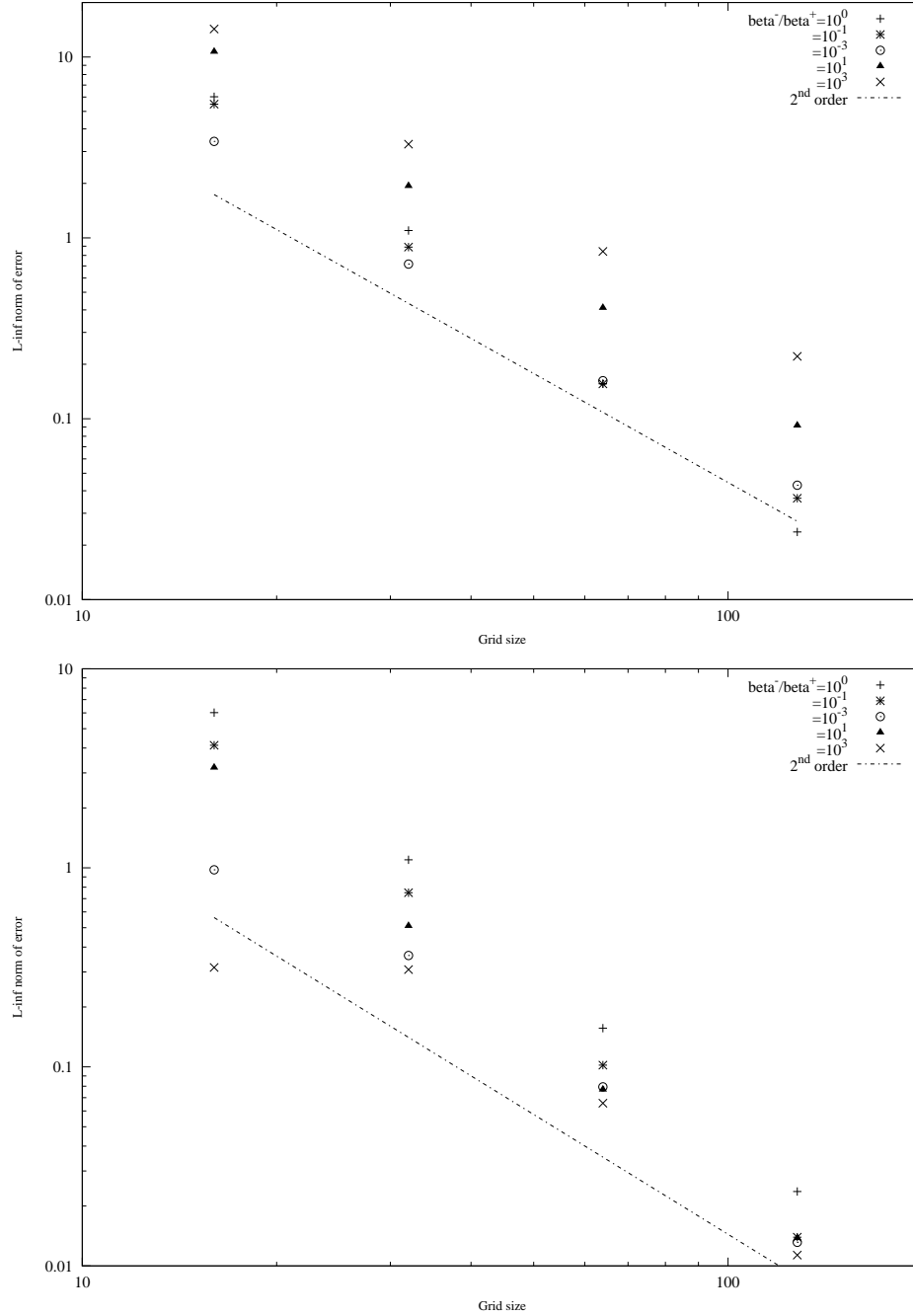


Figure 10: Convergence of the L_∞ norm of the solution error for the heat equation. Top: homogeneous Dirichlet embedded boundary. Bottom: homogeneous Neumann embedded boundary. Results span a range in thermal diffusivity ratios. Black pluses denote a ratio of one. Two cases have larger coefficients outside the sphere, 10^{-1} (*) and 10^{-3} (○). Two cases have larger coefficients inside the sphere, 10^1 (▲) and 10^3 (×). The line is a reference indicating second-order convergence.

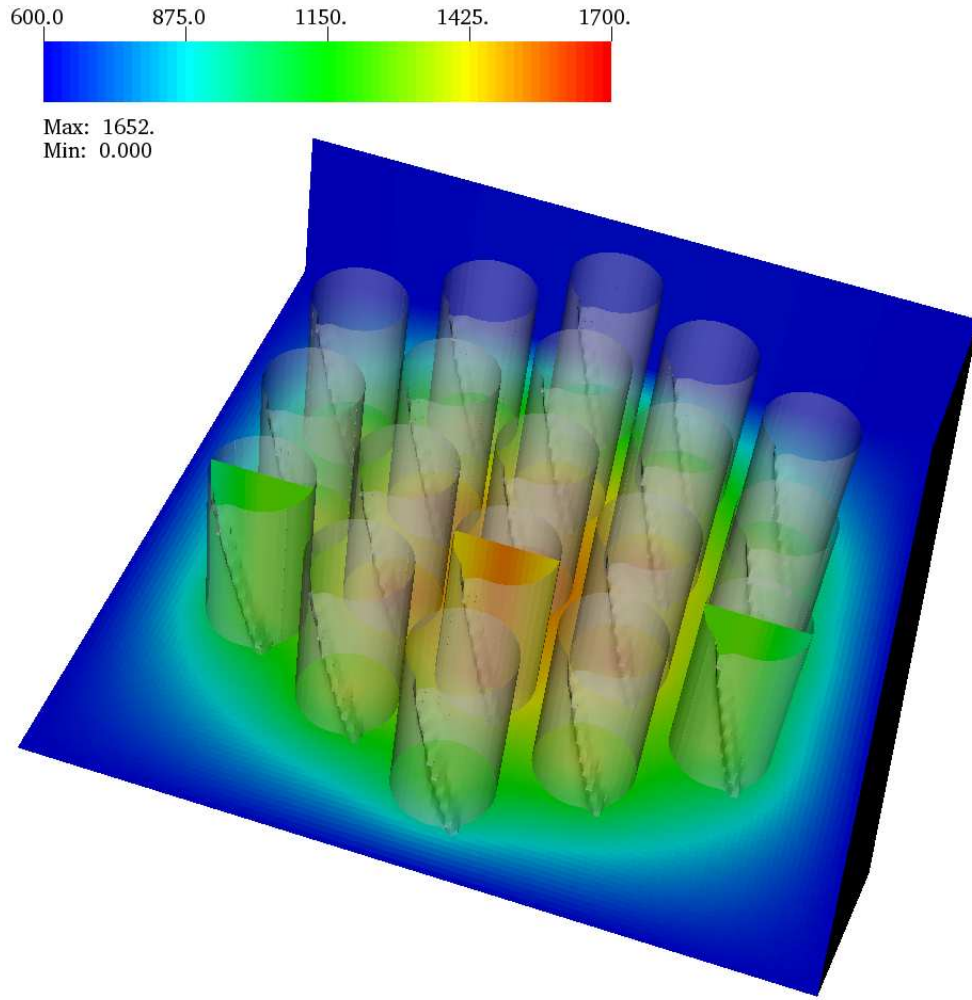


Figure 11: Temperature distribution at steady state for a 19-pin fuel bundle. The interfaces between fuel pin and moderator are represented by semi-transparent surfaces. A slice of the solution inside the third row of pins is shown. The solution on the exterior is shown in a slice at the bottom of the domain.

1
2
3
4
5
6
7
8
9
10
11
12
13
14
15
16
17
18
19
20
21
22
23
24
25
26
27
28
29
30
31
32
33
34
35
36
37
38
39
40
41
42
43
44
45
46
47
48
49
50
51
52
53
54
55
56
57
58
59
60
61
62
63
64
65

Name	value	Source
horizontal domain size	12	None
pin radius	0.800	[20]
wire radius	0.103	[20]
pin-wire separation	0.478	None
pin length	3.000	None
wire separation	20.0	[20]
pin+wire thermal diffusivity	0.9007	[10]
moderator density	0.852	[21]
moderator specific heat	1.2768×10^7	[21]
moderator thermal diffusivity	0.6251	[21]

Table 1: Table of parameters used in fuel bundle test.

6. Conclusions

We have presented an approach to solving elliptic and parabolic equations using Cartesian grid embedded boundary methods which is second order accurate and computationally efficient. The former was achieved using the usual five-point stencil in cells not intersected by the boundary, and a quadratic approximation to the state at the interface otherwise. In order to efficiently solve elliptic equations, we use geometric multigrid. This necessitated treatment of a number of special cases that arise when the geometry is under-resolved.

The method was also shown not to suffer from condition-based solver convergence issues. It remains stable for ratios up to 10^6 . Moreover, we find that the rate of convergence improved at high enough material contrast ratios, a good indicator that it will remain stable and efficient beyond those tested.

The method was tested on a complex nuclear reactor fuel bundle geometry that underscored the flexibility of the grid generation approach. This, along with the parallel computing and AMR capabilities leveraged from Chombo, are essential to approaching large scale problems. In the future, higher order extensions of the underlying method will be explored using both the existing capabilities for high order geometric representations [17] and by extending the stencil approximations to higher order.

7. Acknowledgements

We thank Brian Van Straalen for help with the Chombo software library. This work was supported by the Department of Energy under contract num-

ber DE-AC02-05-CH11231.

References

- [1] G. H. Shortley and R. Weller. The numerical solution of laplace's equation. *Journal of Applied Physics*, 9(5):334–348, 1938.
- [2] Charles S. Peskin. Numerical analysis of blood flow in the heart. *Journal of Computational Physics*, 25(3):220 – 252, 1977.
- [3] Randall J. LeVeque and Zhilin Li. The immersed interface method for elliptic equations with discontinuous coefficients and singular sources. *SIAM Journal on Numerical Analysis*, 31(4):1019–1044, 1994.
- [4] Xu-Dong Liu, Ronald P. Fedkiw, and Myungjoo Kang. A boundary condition capturing method for Poisson's equation on irregular domains. *Journal of Computational Physics*, 160(1):151 – 178, 2000.
- [5] Songming Hou and Xu-Dong Liu. A numerical method for solving variable coefficient elliptic equation with interfaces. *Journal of Computational Physics*, 202(2):411 – 445, 2005.
- [6] Anita Mayo. The rapid evaluation of volume integrals of potential theory on general regions. *Journal of Computational Physics*, 100(2):236 – 245, 1992.
- [7] Leslie Greengard and June-Yub Lee. Electrostatics and heat conduction in high contrast composite materials. *Journal of Computational Physics*, 211(1):64 – 76, 2006.

- [8] Mark S. Day and John B. Bell. Numerical simulation of laminar reacting flows with complex chemistry. *Combustion Theory and Modelling*, 4(4):535 – 556, 2000.
- [9] F. Nicoud. Conservative high-order finite-difference schemes for low-mach number flows. *Journal of Computational Physics*, 158(1):71 – 97, 2000.
- [10] William D. Henshaw and Kyle K. Chand. A composite grid solver for conjugate heat transfer in fluid-structure systems. *Journal of Computational Physics*, 228(10):3708 – 3741, 2009.
- [11] M. Oevermann and R. Klein. A cartesian grid finite volume method for elliptic equations with variable coefficients and embedded interfaces. *Journal of Computational Physics*, 219(2):749 – 769, 2006.
- [12] M. Oevermann, C. Scharfenberg, and R. Klein. A sharp interface finite volume method for elliptic equations on cartesian grids. *Journal of Computational Physics*, 228(14):5184 – 5206, 2009.
- [13] Hans Johansen and Phillip Colella. A Cartesian grid embedded boundary method for Poisson’s equation on irregular domains. *Journal of Computational Physics*, 147(1):60 – 85, 1998.
- [14] Peter McCorquodale, Phillip Colella, and Hans Johansen. A Cartesian grid embedded boundary method for the heat equation on irregular domains. *Journal of Computational Physics*, 173(2):620 – 635, 2001.
- [15] Peter Schwartz, Michael Barad, Phillip Colella, and Terry Ligocki. A cartesian grid embedded boundary method for the heat equation

and poisson's equation in three dimensions. *Journal of Computational Physics*, 211(2):531 – 550, 2006.

- [16] Michael. J. Aftosmis, Marsha J. Berger, and John E. Melton. Robust and efficient cartesian mesh generation for component-based geometry. *AIAA Journal*, 36(6):952 – 960, 1998.
- [17] T J Ligocki, P O Schwartz, J Percelay, and P Colella. Embedded boundary grid generation using the divergence theorem, implicit functions, and constructive solid geometry. *Journal of Physics: Conference Series*, 125:012080 (5pp), 2008.
- [18] E.H. Twizell, A.B. Gumel, and M.A. Arigu. Second-order, L0-stable methods for the heat equation with time-dependent boundary conditions. *Advances in Computational Mathematics*, 6(1):333 – 352, 1996.
- [19] Zhilin Li. A fast iterative algorithm for elliptic interface problems. *SIAM Journal on Numerical Analysis*, 35(1):230–254, 1998.
- [20] Kurt D. Hamman and Ray A. Berry. A CFD process for fast reactor fuel assemblies. In *Experiments and CFD Code Applications to Nuclear Reactor Safety (XCFD4NRS 2008)*, 2008.
- [21] J. K. Fink and L. Leibowitz. Thermodynamic and transport properties of sodium liquid and vapor. Technical Report ANL/RE-95/2, Argonne National Laboratory, 1995.
- [22] R. B. Pember, L. H. Howell, J. B. Bell, P. Colella, W. Y. Crutchfield, W. A. Fiveland, and J. P. Jessee. An adaptive projection method for

unsteady, low-mach number combustion. *Combustion Science and Technology*, 140(1):123 – 168, 1998.

- [23] Frederic Gibou, Ronald P. Fedkiw, Li-Tien Cheng, and Myungjoo Kang. A second-order-accurate symmetric discretization of the Poisson equation on irregular domains. *Journal of Computational Physics*, 176(1):205 – 227, 2002.
- [24] Shaozhong Deng, Kazufumi Ito, and Zhilin Li. Three-dimensional elliptic solvers for interface problems and applications. *Journal of Computational Physics*, 184(1):215 – 243, 2003.
- [25] Y.C. Zhou, Shan Zhao, Michael Feig, and G.W. Wei. High order matched interface and boundary method for elliptic equations with discontinuous coefficients and singular sources. *Journal of Computational Physics*, 213(1):1 – 30, 2006.
- [26] A. McKenney, L. Greengard, and A. Mayo. A fast poisson solver for complex geometries. *Journal of Computational Physics*, 118(2):348 – 355, 1995.